Check for updates

Investigation of desorption of hydrogen gas from polymer matrix using thermal desorption analysis and finite element modeling

Shank S. Kulkarni [a,b,*], Yongsoon Shin [a], Kyoo Sil Choi [a], Kevin Simmons [a]

[a] *Pacific Northwest National Laboratory, Richland, WA 99354, USA*
[b] *The University of Tennessee, Knoxville, TN 37996, USA*

ARTICLE INFO

ABSTRACT

Polymer materials are used widely as sealing materials and liners in hydrogen storage and transportation infrastructure. During operating conditions, polymers are exposed to high pressure hydrogen gas periodically. When in contact, the hydrogen gas diffuses through the polymer material with ease due to its smaller sized molecules compared to the polymer molecules. In the event of rapid decompression of outside hydrogen gas, the hydrogen molecules within the polymer diffuse out. This process is known as the desorption of polymer and can cause blisters or cracking causing permanent damage to the polymer. Here, we used a combined experimental and modeling approach to investigate the desorption of the hydrogen gas in the polymer. Thermal desorption analysis (TDA) experiments were performed on the polymer sample exposed to the high-pressure hydrogen gas to measure the diffusion coefficient and equilibrium hydrogen concentration. Experiments also provided the quantity of hydrogen within the polymer during the desorption process which followed Fick's law. However, for higher pressurization values, some anomaly was observed in the quantity of hydrogen remaining in the polymer sample. A continuum mechanics based coupled diffusion–deformation-damage model was deployed to simulate the gas desorption process in the material using the finite element method to understand its effect on the material. It was found that the anomaly in TDA results were due to the blister formation on the polymer surface which resulted in longer hydrogen retention. Simulations also showed that blister formation can be affected by multiple parameters such as the addition of filler particles, and pre-existing cavity size.

1. Introduction

A significant portion of the global energy currently used comes from fossil fuels which come with consequences of global warming and greenhouse gas emission [1]. A tremendous effort is underway to reduce the dependence on these limited and polluting traditional fuels by generating energy with more environmentally friendly resources. Out of multiple alternatives, the use of hydrogen gas as fuel is emerging as one of the best alternatives to fossil-based fuels. Although hydrogen gas can be obtained from fossil-based raw materials, it can be also generated using multiple clean energy sources such as solar, wind, hydro, and nuclear energy. As the use of hydrogen fuel begins increasing in multiple industries so is the need to develop new infrastructure for a wide use of this new fuel [2–8].

The most common method for storing hydrogen in the infrastructure is in high pressure cylinders as it is currently the most efficient method for storage [9–12]. Unfortunately, high pressure hydrogen gas permeates through almost all materials due to its small size of molecules. When permeated through metal, hydrogen forms metal hydrides which can degrade the mechanical properties of metals without

proper material selection or design that can lead to eventual damage or failure [13–16]. On the other hand, when permeated through organic materials such as rubbers and plastics the hydrogen stays as a diatomic gas and does not form any chemical bonds but can cause influence on morphological structure or cause mechanical damage due to a phenomenon known as 'rapid decompression failure (RDF)' or 'eXplosive decompression failure (XDF)'. In RDF, high pressure hydrogen gas diffuses into the polymer and occupies free volume space and preexisting cavities or voids inside the polymer material. When the applied hydrogen pressure is reduced with a high decompression rate, hydrogen gas trapped inside the cavities does not get sufficient time to diffuse out of the material or cavities and rather escapes by blistering or rupturing the material, causing permanent damage [17–19]. This damage due to RDF is observed in many polymer based components used in hydrogen infrastructure such as dispensing hoses, O-rings, and inner linings of hydrogen storage tanks inside the hydrogen vehicle [20–23]. An improved understanding requires a more in-depth investigation of this failure mode so that new polymer materials can be developed for use

in the hydrogen infrastructure for a more reliable and robust material system. Measurement of hydrogen gas transport properties such as the diffusivity of hydrogen through polymer material is important for this investigation.

Ethylene propylene diene monomer (EPDM), nitrile butadiene rubber (NBR), and fluoroelastomer (FKM) are some of the most widely used polymers in the hydrogen infrastructure. A lot of research has been conducted on the behavior of these materials when exposed to high pressure gas. Yamabe et al. [24,25] were the first ones to study the effect on EPDM and NBR due to exposure to high pressure hydrogen gas. They also conducted experiments on the variants of polymers by adding filler particles and plasticizers in the pure EPDM and NBR and found the damage due to RDF reduces drastically with the addition of filler particles. In a separate study, Yamabe [26] conducted experiments to study the effect of temperature on the performance of O-rings made of EPDM polymer which showed that the damage is directly related to the ambient temperature. Jaravel et al. [17] investigated the effect of applied hydrogen pressure and depressurization rate on cavity expansion and showed that both of these parameters play an important role in deciding the cavity's appearing time during decompression. Kane et al. [27] further experimented and were successful in tracking the growth of a single cavity within transparent EPDM during multiple pressurization–depressurization cycles. Fujiwara et al. [28] used infrared and Raman measurements to study the chemical degradation within NBR. They did not find any evidence of structural changes in NBR such as hydrogenation of the olefinic bonds in butadiene or of the cyano groups in acrylonitrile proving the failure was only mechanical. Hence, they further studied the effect of silica fillers in NBR on the mechanical degradation during multiple pressure cycles of hydrogen gas [29]. The volume change during the decompression of hydrogen gas was studied by Castagnet et al. [30] by carefully removing the effect of thermal expansion and the compressibility contributions. Ono et al. [31] showed that the damage during RDF accumulates over multiple pressurization–depressurization cycles leading to large cracks eventually resulting in the failure of the component. Multiple imaging techniques were also used to investigate the evolution of cavities during decompression such as small angle X-ray scattering [32], X-ray tomography [33], in-situ X-ray tomography [34], and optical micrographs [35].

Many researchers approached the RDF from a modeling perspective and conducted simulations to understand the decompression process better. Lopez et al. [36,37] developed a cavitation criterion for elastomers by considering the sudden growth of the existing defect within the material. This work was later used by Lefevre et al. [38,39] to model the cavitation phenomenon in natural rubber and the transformation of micro cracks to macro cracks. Jaravel et al. [18] modeled cavity evolution using the elastic modulus of polymer and the coefficient of diffusion of hydrogen through the polymer. Zhou et al. [40,41] performed the simulations at the macroscale to investigate the performance of sealing components using the finite element method (FEM). Formation of blister during RDF was modeled by Yersak et al. [22] with the help of Henrys law, Ficks second law, and material yield criterion. Kulkarni et al. [42–44] modeled EPDM polymer as hyperelastic material to predict the damage initiation during RDF. They also performed X-ray computed tomography (XCT) on EPDM samples exposed to high pressure hydrogen to qualitatively validate the simulation results. More details about modeling efforts to predict the failure in high-pressure hydrogen storage tanks can be found in a review paper by Zhang et al. [45].

In this study, we used a combined experimental and modeling approach to investigate the desorption of hydrogen in polymer during RDF. We used an ex-situ thermal desorption analysis-gas chromatography (TDA-GC) method to obtain the diffusivity of hydrogen through EPDM. This method has been used in past by Jung et al. [46] to evaluate the hydrogen permeation characteristics in the EPDM material. The amount of hydrogen leaving the polymer was measured in this method

and using Fick's law, the coefficient of diffusion was obtained from that information. The quantity of hydrogen diffusioning from the polymer sample was found to obey Fick's law with some exceptions for higher pressure values. Two additional variants of pure EPDM were also studied, one with added plasticizer and one with added carbon black (CB) fillers. The addition of fillers was found to increase the coefficient of diffusion of the EPDM polymer whereas the addition of plasticizer was found to decrease the coefficient of diffusion. Obtained experimental values were then used in the coupled diffusion–deformation-damage model to simulate the hydrogen desorption process. The finite element method was chosen to deploy the coupled model due to its robust nature and ability to handle complex geometries [47,48]. The simulation results were able to predict the trends obtained via experiments and provided insight into stress, strain, and hydrogen concentration distribution during the hydrogen desorption. Simulation results show that the reason for a sudden increase in the hydrogen retention of polymer was due to blister formation which resulted in additional resistance for hydrogen gas diffusing out.

This paper is organized as follows. The manuscript begins with Section 1 which provides a brief introduction about the past work related to the rapid decompression failure along with the motivation for this study. Section 2 provides detailed information about the experimental work of Thermal Desorption Analysis (TDA) along with Gas Chromatography (GC). Next, Section 3 gives the basic theoretical concepts needed to understand the model followed by the coupled diffusion–deformation-damage model. Section 4 gives the details of materials used in this study along with the material parameters used in simulations. The finite element model is then described in Section 5. The following section, Section 6, contains all the experimental and simulation results using coupled model along with the discussion of results. Finally, the manuscript concludes with some remarks in Section 7.

2. Thermal desorption analysis

The main purpose of the TDA along with GC experiments was to measure diffusion coefficient (D), equilibrium hydrogen concentration (C_0), and hydrogen solubility. The quantity of hydrogen gas leaving the polymer specimen with respect to time can also be measured using these experiments. The schematic diagram of the TDA-GC process is shown in Fig. 1. The overall experimental process can be summarized below:

1. A polymer specimen needs to be cut in a cylinder form and its diameter, thickness, density, and weight should be measured before inserting it in the hydrogen exposure chamber. A diameter of a specimen should be smaller than a pressure vessel diameter because sometimes a polymer specimen would be significantly swelled during the decompression depending on the decompression rate.

2. After the specimen is loaded inside the hydrogen exposure chamber, the chamber is evacuated and purged with helium three times. Then the chamber is charged with ultrapure hydrogen gas (99.999%) up to a desired pressure and a pressure gauge should be checked to see if there is a leak after the hydrogen cylinder is closed. The chamber pressure needs to be checked from time to time until decompression (24 h).

3. After 24 h of pressurization, the hydrogen exposure chamber is opened under control for the decompression (pressure drop/time: time should be recorded right after the pressure starts to drop). Once the hydrogen pressure drops to zero, the chamber should be purged with argon or helium gas to make sure that the specimen does not get exposed to air. The time between starting the chamber decompression and the specimen loading to the oven should be recorded because it will be considered during the calculation of D and C_0. Usually, this induction time is about 10 min.
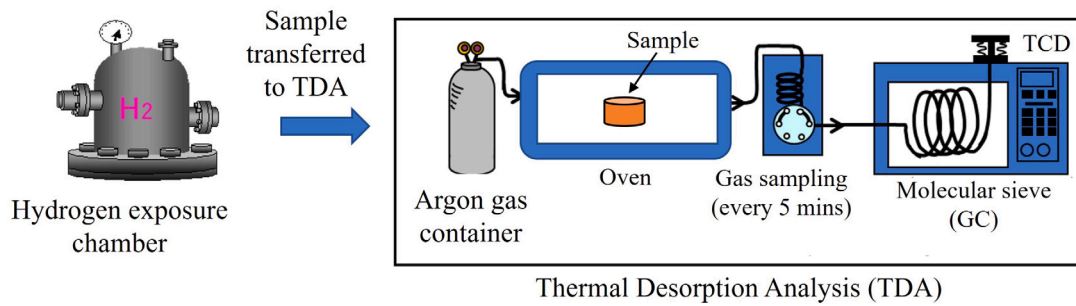
Fig. 1. Schematic diagram of thermal desorption analysis.

4. During the decompression of the chamber, the TDA-GC system (Argon cylinder connected to 30 degrees C (303 K) oven, a sample holder inside the oven) should be ready. Argon gas flow should be 50 mL/min consistently during the whole analysis. Micro GC collects gas released from the sample every 4–5 min and analyzes. The sample is then moved to the oven from hydrogen exposure chamber for the measurements of thermal desorption analysis.

5. TD measurement is continued until hydrogen content of at least 10 measurements is zero.

Fig. 2 shows the experimental setup of the TDA-GC experiments carried out in this study. Hydrogen content recorded in GC is molar % in argon mixture. Therefore, first it should be converted to molar ppm and then to the wt. ppm. First, using the gas equation, the total number of moles of the mixed gas in the sample loop should be calculated as

$$n = \frac{PV}{RT}, \tag{1}$$

where n is number of moles, volume V is GC column volume (0.25 mm $\times$ 10 mm), gas constant R is 8.20544 $\times$ 10^{-5} atm/mol K, pressure P is 1 atm, and temperature T is 303 K. This results in the value of $n = 1.973355 \times 10^{-5}$ mol. The number of moles (molar ppm) of H_2 gas in the mixed gas can be calculated as

$$n_{H_2} = C ppm \times (n_{H_2} + n_{Ar}) = C ppm \times n, \tag{2}$$

where n_{H_2} and n_{Ar} are the number of moles of hydrogen and argon, respectively. It should be noted that Micro GC automatically calculates H_2 mol% once calculated with calibration gas mixture.

Second, the mass (molar ppm) of hydrogen is converted to a wt ppm unit. The mass concentration of H_2 released/s for each GC measurement for 1 injection (wt ppm/s) is,

$$C\left(\frac{\text{wt. ppm}}{s}\right) = \frac{C_{mol} P m_{H_2} v_{Ar}}{m_{sample} RT}, \tag{3}$$

where, $v_{Ar} = 50$ mL/min $= 8.33 \times 10^{-7}$ m^3/s.

By substituting the values of P, m_{H_2}, v_{Ar}, R, and T in Eq. (3), we get

$$C\left(\frac{\text{wt. ppm}}{s}\right) = 6.890 \times 10^{-5} \frac{C_{mol}}{m_{sample}}. \tag{4}$$

When wt. ppm of hydrogen gas released from the specimen is plotted as a function of time, a plateau occurs which is the equilibrium concentration (C_0) of hydrogen in the specimen. A plot of wt. ppm of hydrogen gas remaining in sample as a function of time derived can be obtained and this plot needs to be fitted into the gas diffusion equation,

$$C_t = \frac{32}{\pi^2} C_0 \left[\sum_{n=0}^{\infty} \frac{e^{(-(2n+1)^2 \pi^2 D \frac{t}{z^2})}}{(2n+1)^2} \right] \left[\sum_{n=1}^{\infty} \frac{e^{(-D\beta_n^2 \frac{t}{r^2})}}{\beta_n^2} \right], \tag{5}$$

to find out diffusion coefficient (D) of the specimen [24,46]. Where C_t is the remaining hydrogen content (ppm), D is diffusion coefficient

(m^2/s), z is the thickness of the sample, and r is the radius of the sample. β_n is the root of the zero-order Bessel function. With the first six roots as $\beta_1 = 2.405$; $\beta_2 = 5.524$; $\beta_3 = 8.654$; $\beta_4 = 11.792$; $\beta_5 = 14.931$; $\beta_6 = 18.071$ sufficiently accurate values can be computed readily for most cases.

3. Theoretical background

3.1. Diffusion equation

Diffusion of hydrogen through polymer can be described by Fick's first law of mass diffusion in 3D which states that the diffusion flux is directly proportional to the concentration gradient as

$$\boldsymbol{J} = -D\left(\frac{\partial c}{\partial x}\hat{e}_x + \frac{\partial c}{\partial y}\hat{e}_y + \frac{\partial c}{\partial z}\hat{e}_z\right), \tag{6}$$

where $\boldsymbol{J}$ is the diffusion flux vector, D is the coefficient of diffusion, and c is the concentration. Also, $\frac{\partial}{\partial x}$, $\frac{\partial}{\partial y}$, and $\frac{\partial}{\partial z}$ are first order partial derivatives with respect to x, y, and z where (x, y, z) are the Cartesian coordinates, and $\hat{e}_x$, $\hat{e}_x$, and $\hat{e}_x$ are unit vectors along x, y, and z directions respectively. The –ve sign in this equation indicates that the diffusion will always take place from high to low concentration regions and not in reverse.

Fick's second law, which can be derived from the first law and the law of mass conservation, describes the change of concentration with respect to time and is given by

$$\frac{\partial c}{\partial t} = D\left(\frac{\partial^2 c}{\partial x^2} + \frac{\partial^2 c}{\partial y^2} + \frac{\partial^2 c}{\partial z^2}\right), \tag{7}$$

where $\frac{\partial}{\partial t}$ is the time derivative, $\frac{\partial^2}{\partial x^2}$, $\frac{\partial^2}{\partial y^2}$, and $\frac{\partial^2}{\partial z^2}$ are second order partial derivatives with respect to x, y, and z coordinates respectively.

3.2. Basic kinematics for finite deformation

A deformation gradient tensor, usually denoted by $\boldsymbol{F}$, is an important parameter that provides a relationship between vectors in the reference and current configurations when a continuum body deforms. The deformation gradient can be used to define strain measures in the body and the determinant ($J = det\boldsymbol{F}$) of the deformation gradient is also equal to the change in volume of the material point.

The right Cauchy–Green tensor ($\boldsymbol{C}$) and the left Cauchy–Green tensor ($\boldsymbol{B}$) are related to the deformation gradient $\boldsymbol{F}$ by

$$\boldsymbol{C} = \boldsymbol{F}^T \cdot \boldsymbol{F} \quad \text{and} \quad \boldsymbol{B} = \boldsymbol{F} \cdot \boldsymbol{F}^T. \tag{8}$$

The right and left Cauchy–Green deformation tensors also have squares of the principal stretch as eigenvalues denoted by $\lambda_i^2, i = 1, 2, 3$, where λ_i are principal stretches. The invariants of both the tensors $\boldsymbol{B}$ and $\boldsymbol{C}$ are equal to each other and can be given in terms of the principal stretches as

$$I_1 = I_1(\boldsymbol{C}) = I_1(\boldsymbol{B}) = \lambda_1^2 + \lambda_2^2 + \lambda_3^2, \tag{9a}$$
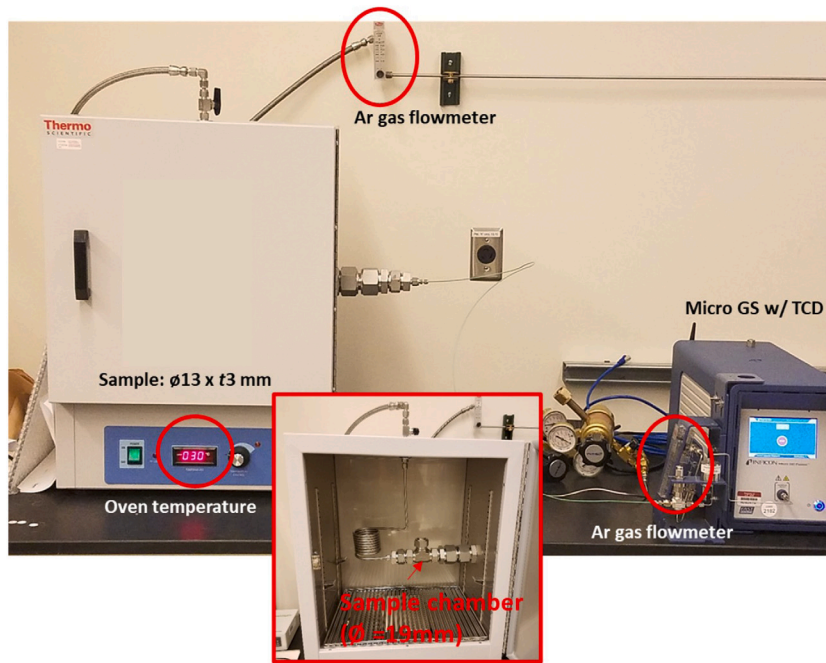
Fig. 2. Thermal desorption analysis experimental setup.

$$I_2 = I_2(\boldsymbol{C}) = I_2(\boldsymbol{B}) = \lambda_1^2 \lambda_2^2 + \lambda_2^2 \lambda_3^2 + \lambda_3^2 \lambda_1^2, \tag{9b}$$

$$I_3 = I_3(\boldsymbol{C}) = I_3(\boldsymbol{B}) = J^2 = \lambda_1^2 \lambda_2^2 \lambda_3^2. \tag{9c}$$

A special case of uniaxial loading can be considered as the experimental uniaxial stress strain curve is easy to obtain. The polymer can be treated as incompressible material which leads to the value of J being equal to 1. In terms of principal stretches, it can be written as

$$J = \lambda_1 \lambda_2 \lambda_3 = 1. \tag{10}$$

Assuming the principal stretch in the direction of loading as λ_1, for isotropic material under uniaxial loading, the other two principal stretches must be equal to each other and can be given as

$$\lambda_2 = \lambda_3 = \lambda_1^{-1/2}. \tag{11}$$

Therefore, the three invariants of tensor $\boldsymbol{B}$ can be written as

$$I_1 = \lambda_1^2 + \lambda_2^2 + \lambda_3^2 = \lambda_1^2 + 2\lambda_1^{-1}, \tag{12a}$$

$$I_2 = \lambda_1^2 \lambda_2^2 + \lambda_2^2 \lambda_3^2 + \lambda_3^2 \lambda_1^2 = \lambda_1^{-2} + 2\lambda_1, \tag{12b}$$

$$I_3 = \lambda_1^2 \lambda_2^2 \lambda_3^2 = 1. \tag{12c}$$

3.3. Hyper-elastic material model

Hyperelastic material models are based on the existence of a strain energy density function W defined per unit reference volume. Usually, these models are used to model the mechanical response of rubber-like materials which undergo large elastic deformations without any permanent or plastic deformation.

Multiple different forms of strain energy density functions have been proposed in the past. Some of the popular strain energy density functions are Neo-Hookean [49], Arruda–Boyce [50], Mooney–Rivlin [51,52], Yeoh [53], and Ogden [54]. For EPDM polymer, the Ogden model is the most widely used model hence used in this study [55,56].

According to the Ogden model, the strain density function can be written as [54]

$$W = \sum_{j=1}^{n} \frac{\mu_j}{\alpha_j} \left(\lambda_1^{\alpha_j} + \lambda_2^{\alpha_j} + \lambda_3^{\alpha_j} - 3 \right), \tag{13}$$

where μ_j are constant shear moduli, α_j are dimensionless constants, $(\lambda_1, \lambda_2, \lambda_3)$ are principal stretches and n is the number of terms in the strain energy function. The values of material parameters μ_j, α_j, and n can be found by curve fitting the Eq. (13) on the mechanical response of polymer obtained via experiments.

3.4. Maximum principal strain failure theory

As reported in our earlier studies, EPDM polymer and its variants undergo sudden fracture during uniaxial tensile test [42]. The maximum principal strain failure theory can predict this sudden failure and it states that fracture occurs when the maximum principal strain for a complex state of the stress system becomes equal to or exceeds the strain at the fracture point in the uniaxial tensile test.

In the case of two-dimensional loading condition, the maximum principal strain can be given as

$$\varepsilon_{max} = \frac{\varepsilon_{xx} + \varepsilon_{yy}}{2} + \sqrt{\left(\frac{\varepsilon_{xx} - \varepsilon_{yy}}{2}\right)^2 + \left(\frac{\gamma_{xy}}{2}\right)^2}, \tag{14}$$

where ε_{max} is the maximum principal strain at any point in the body and ε_{xx}, ε_{yy}, and γ_{xy} are strain components at the same point. According to the maximum principal strain failure theory, the fracture will occur at a material point where the following condition is met:

$$\varepsilon_{max} \geq \varepsilon_f, \tag{15}$$

where ε_f is the strain at the fracture point in a uniaxial tensile test.

3.5. Coupling between diffusion and deformation

Diffusion of hydrogen through polymer is assumed to cause purely dilatational strain at any point in a body that is linearly proportional to the change in hydrogen concentration. It can be given as

$$\varepsilon_{ij}^H = \alpha_H \Delta c \delta_{ij}, \tag{16}$$

where, ε_{ij}^H is hydrogen-induced strain, α_H is the linearity proportional constant, δ_{ij} is Kroneckers delta, and Δc is the change in the hydrogen concentration.
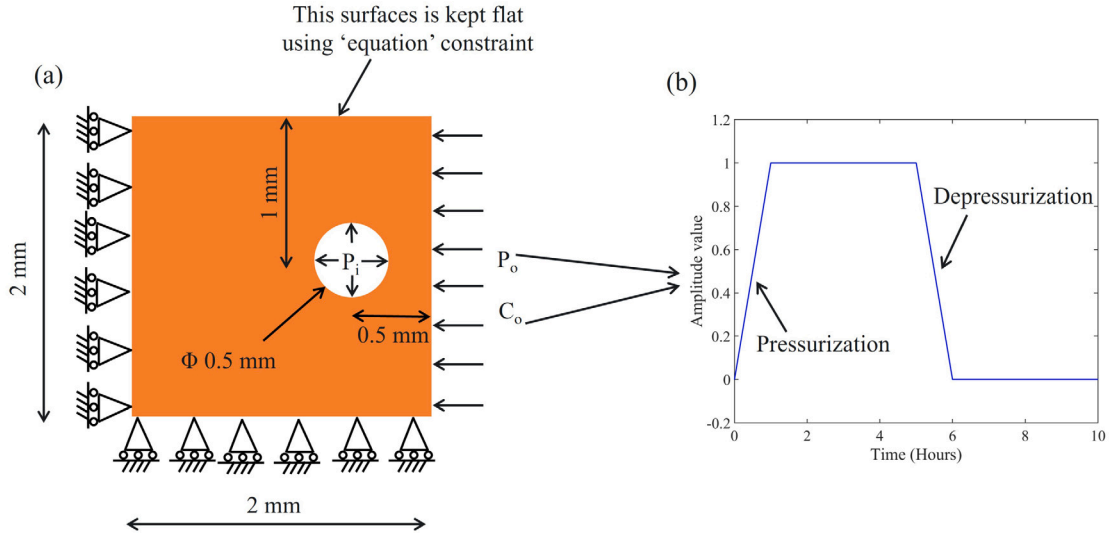
Fig. 3. Finite element model setup of an RVE with cavity. (For interpretation of the references to color in this figure legend, the reader is referred to the web version of this article.)

Table 1
Similarity between diffusion equation and heat transfer equation [44,57].

	Diffusion equation	Heat equation
Balance law	$\frac{\partial c}{\partial t} + \nabla \cdot J_m + r_m$	$\rho C_p \frac{\partial T}{\partial t} + \nabla \cdot J_q + r_q$
Degree of freedom	Concentration c	Temperature T
Source	Mass source r_m	Heat source r_q
Flux	Mass flux r_m	Heat flux r_q
Coefficient	D	$\frac{k}{\rho C_p}$

The total strain at any point within the material can be decomposed into two parts as

$$\varepsilon_{ij} = \varepsilon_{ij}^e + \varepsilon_{ij}^H, \tag{17}$$

where ε_{ij} is the total strain and ε_{ij}^e is the hyperelastic strain. Using Eq. (17) both diffusion as well as mechanical equilibrium equations are coupled to each other.

3.6. Correlation with heat equation

State of the art commercial FEM software does not provide the option of performing coupled diffusion–deformation simulations to the user. Although some software such as Abaqus does have provision to implement this coupled model with the help of a user element subroutine (UEL), it is a challenging task that requires meticulous programming work. In order to keep the implementation of the presented coupled diffusion–deformation-damage model fairly simple, we can use already existing coupled heat transfer-deformation elements in Abaqus. These elements have an additional degree of freedom for each node that represents temperature. Due to the similarity between the heat equation and diffusion equation, we can also treat the temperature degree of freedom as the concentration degree of freedom [57]. The similarity between both equations is shown in Table 1 and has been used by multiple researchers in the past [58–62].

The heat equation can be given as

$$\rho C_p \frac{\partial T}{\partial t} = k \left(\frac{\partial^2 T}{\partial x^2} + \frac{\partial^2 T}{\partial y^2} + \frac{\partial^2 T}{\partial z^2} \right), \tag{18}$$

where T is temperature, ρ is the material density, C_p is specific heat, and k is the thermal conductivity of the material. Eq. (18) shows heat equation whereas Eq. (7) shows diffusion equation. By replacing the

temperature T with concentration c, we can get the relation between parameters from both equations:

$$\frac{k}{\rho C_p} = D. \tag{19}$$

Therefore, both diffusion and heat equations can be used interchangeably if parameters satisfy Eq. (19).

4. Materials used and model parameters

A total of three EPDM model compounds were used for this study. All model EPDM materials (i.e., pure EPDM, plasticized EPDM, and filled EPDM) were purchased from Takaishi Industry, Japan. The details of compound composition are given in Table 2.

All the hyperelastic Ogden model material parameters were found out by curve fitting the uniaxial stress–strain curve of unexposed polymer for three variants of EPDM polymer [42]. The fracture strain values were also calculated based on uniaxial tensile tests. The mechanical properties of the polymer might change with respect to the quantity of hydrogen present in it. In order to obtain those properties, in situ testing such as tensile tests must be performed which was out of the scope of this study due to the limitations of experimental facilities. Hence it was assumed that the mechanical properties of the polymer such as hyperelastic material parameters remain the same for any quantity of dissolved hydrogen. But the linearity proportional constant (α_H) changes the hydrogen induced strain resulting in some form of dependence between the quantity of dissolved hydrogen and the stress state in the material. The density of each variant was also measured. For the completeness of the manuscript, all the material parameters are listed in Tables 3, 4, and 5 for pure EPDM, plasticized EPDM, and CB filled EPDM respectively. The diffusion coefficient values will be obtained from TDA-GC analysis.

5. Finite element model

A representative volume element (RVE) of EPDM polymer was chosen for this study as shown in Fig. 3(a). The chosen RVE had a square shape with a length of each side equal to 2 mm. The size of RVE was selected based on the size of cavities observed experimentally during RDF in the past [31,33]. The RVE had a single circular cavity shown by white color in Fig. 3(a). The diameter of the cavity and the location of the cavity from the free surface both were chosen to be 0.5 mm. Here the distance is measured from the center of the cavity to

Table 2
Overview of model EPDM materials for uniaxial tensile testing (Unit PHR (parts per hundred rubber)) [42].

	Pure EPDM	Plasticized EPDM	Filled EPDM
Base material	EPDM (Esprene505[c])	EPDM (Esprene505[c])	EPDM (Esprene505[c])
Features	No fillers No plasticizer	No fillers Plasticizer	Carbon black No plasticizer
Stearic acid	1	1	1
Zinc oxide	5	5	5
Sulfur	1.5	1.5	1.5
MBTS[a]	1.5	1.5	1.5
TMTD[a]	0.7	0.7	0.7
DOS[b]	–	10	–
Carbon black (N330)	–	–	25
Density (g/cm^3)	0.921	0.919	1.013
Hardness (IRHD)	55.3	48.3	67.2

[a]Accelerators–MBTS:2,2-benzothiazyl disulfide, TMTD: bis(dimethylthiocarbamoyl) disulfide.

[b]Plasticizer–DOS: dioctyl sebacate.

[c]Esprene 505 (Sumitomo Chemical): ethylene 50%, propylene 40%, 5-ethylidene-2-norbornene (ENB) 10%; Nipol 1042 (Zeon Corporation): medium high nitrile rubber, acrylonitrile content 33.5%.

Table 3
Deformation model parameters for pure EPDM material [42].

	μ_n	α_n	Fracture strain	Density (gm/cm^3)
1	−1.12414496	1.79096314		
2	0.476377652	3.26267795	1.39	0.921
3	1.90327281	0.04246690177		

Table 4
Deformation model parameters for plasticized EPDM material [42].

	μ_n	α_n	Fracture strain	Density (gm/cm^3)
1	−1.67303036	2.59913393		
2	0.414399166	3.95292010	1.1289	0.919
3	2.27028270	1.46458676		

Table 5
Deformation model parameters for filled EPDM material [42].

	μ_n	α_n	Fracture strain	Density (gm/cm^3)
1	−161.222964	0.112529827		
2	74.4138682	0.665877192	1.9131	1.013
3	89.2586248	−0.511071834		

the free surface as shown in Fig. 3(a). Mixed boundary conditions were applied on the RVE which includes the roller support on the bottom and left edge. The top edge of RVE had been constrained in such a way that displacement in the vertical direction for all the nodes on the top edge was the same at all times. This was achieved using an 'equation' constraint in Abaqus [63]. It is important to ensure this to maintain the periodicity in the vertical direction. The cavity was also prescribed with internal pressure boundary condition with variable pressure value P_i. The value of P_i is directly proportional to the value of hydrogen concentration on the periphery of the cavity. This pressure value was calculated dynamically as the simulation progresses [43].

The right edge of the cavity was considered to be a free surface where hydrogen exposure was applied. This hydrogen exposure was a combination of two boundary conditions P_o and C_o. P_o was mechanical pressure exerted by the outside hydrogen on the polymer RVE and it varied with respect to time as shown by the amplitude curve in Fig. 3(b). Initially, pressurization took place as the value of P_o increases from zero to 7 MPa in 1 h. This pressure was then maintained for the next 4 h followed by depressurization which brings down the value of P_o again back to zero in 1 h. Finally, this zero pressure was again maintained for the next 4 h. At the same time, we need another boundary condition for the diffusion equation in order to solve the coupled model. This boundary condition was again applied on the right edge of the RVE where the hydrogen concentration C_o varied as shown by the

amplitude curve in Fig. 3(b). Application of these boundary conditions was performed using 'Amplitude' feature in Abaqus [63]. The value of P_o and C_o must be related to each other and that relationship was found by TDA experiments which is discussed in the next section.

The RVE was meshed using four noded plane strain quad elements as shown in Fig. 4. These elements (CPE4T) have three active degrees of freedom at each node. A biased seed was used to refine the mesh near the cavity with element size varying from 0.1 mm to 0.02 mm.

All the simulations were performed with the help of an explicit solver from Abaqus [63] due to the high geometric and material model non-linearity. The diffusion equation was integrated using the explicit forward-difference time integration rule as

$$c_{(i)}^N = c_{(i-1)}^N + \Delta t_{(i)} \dot{c}_{(i-1)}^N, \tag{20}$$

where $c_{(i)}^N$ is concentration at node number N at i^{th} increment, $\Delta t_{(i)}$ is current increment size, and $\dot{c}_{(i-1)}^N$ is the time derivative of concentration at node number N at the previous increment. The value of $\dot{c}_{(i-1)}^N$ was calculated at the beginning of each increment as

$$\dot{c}_{(i-1)}^N = (C^{NJ})^{-1}[P_{i-1}^J - F_{i-1}^J], \tag{21}$$

where C^{NJ} is the lumped capacitance matrix, P_{i-1}^J is the applied nodal source vector, and F_{i-1}^J is the internal flux vector from previous step.

On the other hand, the displacement values were obtained using the explicit central-difference integration rule with a diagonal element (also known as 'lumped') mass matrix as

$$\dot{u}_{(i-\frac{1}{2})}^N = \dot{u}_{(i-\frac{3}{2})}^N + \frac{\Delta t_{(i)} + \Delta t_{(i-1)}}{2} \ddot{u}_{(i-1)}^N, \tag{22}$$

$$u_{(i)}^N = u_{(i-1)}^N + \Delta t_{(i)} \dot{u}_{(i-\frac{1}{2})}^N, \tag{23}$$

where u stands for displacement degree of freedom, $\dot{u}$ is velocity, and $\ddot{u}$ is acceleration. Similar to concentration gradient, the acceleration was calculated as

$$\ddot{u}_{(i-1)}^N = (M^{NJ})^{-1}[P_{i-1}^J - H_{i-1}^J], \tag{24}$$

where M^{NJ} is the mass matrix and H^J is the internal force vector. Hence both diffusion and mechanical equilibrium equations were solved simultaneously by an explicit coupling. We normalized time along with the normalization of thermal conductivity with its reciprocal in order to bring down the computational cost of simulations. The obtained solution using normalized time was again converted back to normal time accordingly [43].

The damage model given in Section 3.4 was implemented in the software Abaqus using the VUSDFLD subroutine. The use of this subroutine allows the user to define a new field variable. In this work, the newly defined field variable was given a default value of '0',
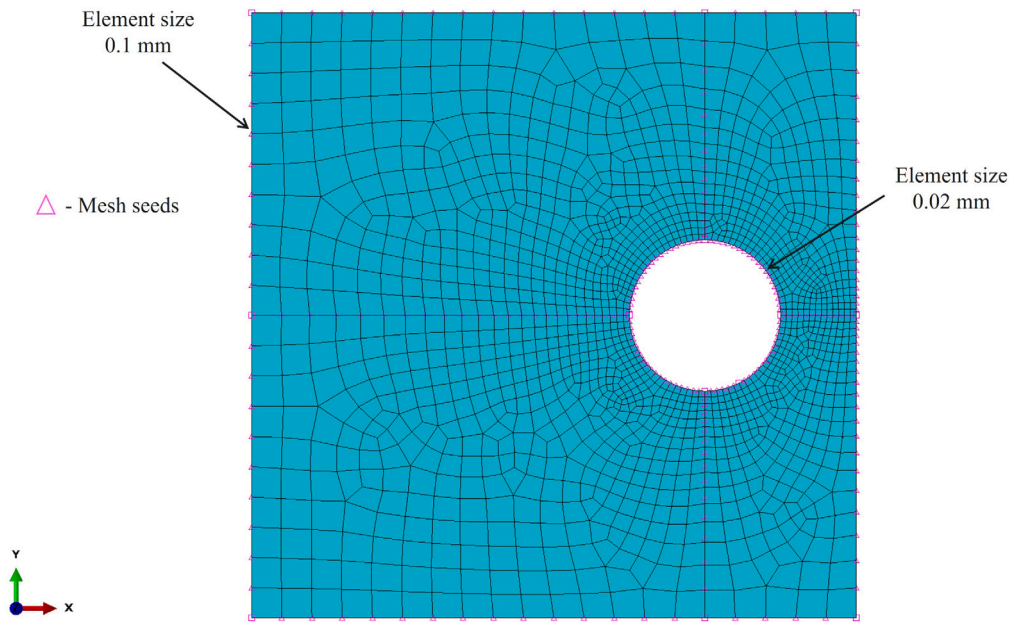
Fig. 4. A typical mesh on the RVE using four noded plane strain quad elements. A biased seed was used to refine the mesh near the cavity.
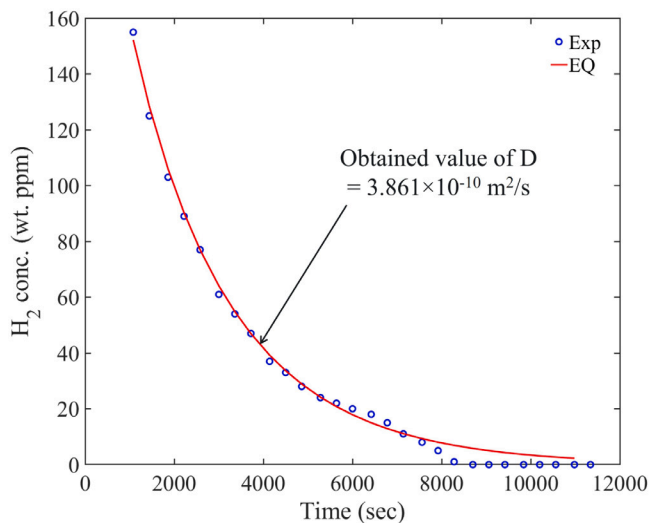

Fig. 5. Results from TDA experiments and fitting of Fick's equation on the data for pure EPDM material sample, with a dimension of ϕ 13 mm × 3 mm thick. The sample was exposed to hydrogen gas with a pressure 12 MPa and desorption was conducted at 303 K temperature.

Table 6
Experimental results for the coefficient of diffusion obtained via fitting of Eq. (5) for three variants of EPDM polymer.

	Material variant	Diffusion coefficient (m²/s)
1	Pure EPDM	3.861×10^{-10}
2	Plasticized EPDM	4.089×10^{-10}
3	Filled EPDM	2.97×10^{-10}

was 2.5 MPa/min. Results show that the total H_2 content of the sample was about 160 wt. ppm, when transferred to the CG-TDA chamber, and the sample retained the hydrogen for around 7 h. Eq. (5) was fitted into obtained data and the value of diffusion coefficient was found to be 3.861×10^{-10} m²/s. A close fit was achieved with the value of R^2 being close to 0.99. Similar data were obtained for the other two variants of EPDM as well and results for the coefficient of diffusion are given in Table 6. It was found that with the addition of plasticizer, the diffusivity of hydrogen did not change significantly but with the addition of CB fillers diffusivity decreased. This is most likely due to the added resistance to the hydrogen flow in the form of filler particles. Once analysis was completed and the sample was taken out, it looks the same as the initial sample on the macroscale. On the micro scale, some cracks and damage was observed which was reported in detail in our separate manuscript [42].

Similar TDA experiments were repeated for different values of pressurization ranging from 7 MPa to 27.6 MPa and corresponding results for pure EPDM material are shown in Fig. 6. Eq. (5) was fitted using all four curves at different pressure values and corresponding values of diffusion of coefficient D are given in Table 7. The value of the coefficient of diffusion was almost the same in all four cases showing that the coefficient of diffusion for EPDM polymer is not affected by applied hydrogen pressure. As the pressure value increased, the total initial hydrogen concentration also increased. The overall curve followed Fick's law with some exceptions which can be easily observed for a pressure value of 27.6 MPa as seen in Fig. 6. Around 4000 s time, a sudden increase in the hydrogen retention of the sample was observed which again went down as time progressed. Although this anomaly was observed for other lower pressure values as well but its intensity was negligible. Only at higher pressure values this hump-like feature was clearly visible. To further investigate this phenomenon, FEM simulations were carried out of hydrogen desorption of EPDM.
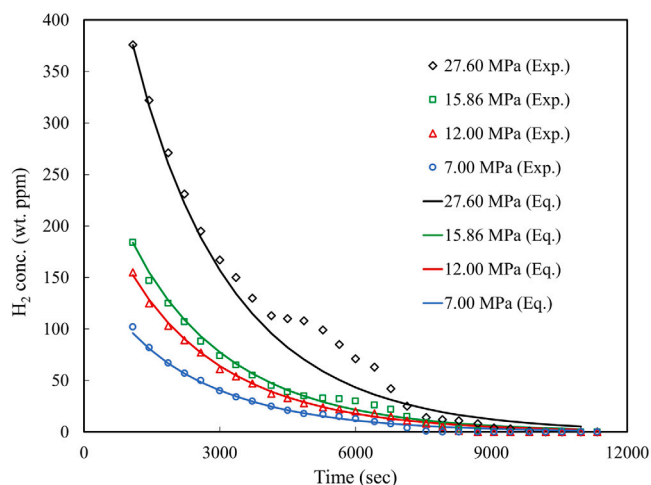
which means intact material. At each increment, the value of maximum principal strain was calculated using Eq. (14) and compared with the material's fracture strain. If the condition given in the Eq. (15) was satisfied then the value of the field variable was changed to 1 indicating full failure. The elements with damage parameter value 1, were deleted using the DEPVAR material parameter option. This breaks the element connectivity and damage propagates.

6. Results and discussion

6.1. TDA-GC experiment results

Fig. 5 shows the amount of hydrogen remaining in the pure EPDM sample during desorption of polymer with respect to time for pressurization done up to 12 MPa. The decompression rate of these samples

Fig. 6. Results from TDA experiments for pure EPDM material samples (Cylindrical sample with ϕ 13 mm × 3 mm thick) at different levels of pressurization. The desorption analysis was conducted at 303 K temperature.
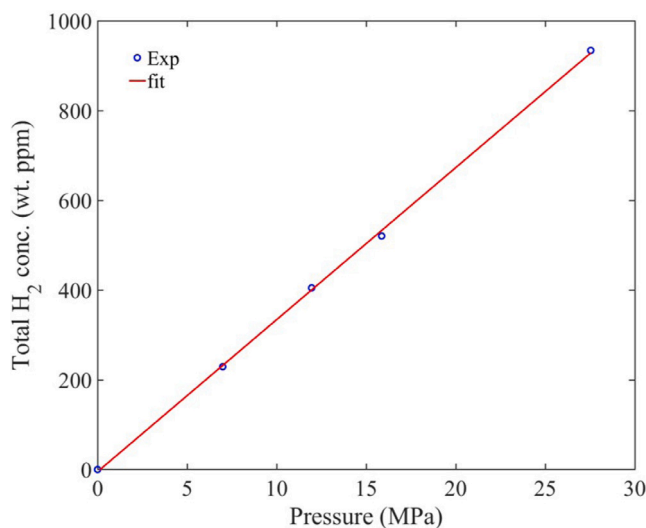

Fig. 7. Relation between hydrogen pressure and total hydrogen concentration.

Table 7

Values of coefficient of diffusion D obtained using different levels of pressurization for pure EPDM material.

Sr. No.	Hydrogen pressure (MPa)	Diffusion coefficient (m^2/s)
1	7.0	3.715×10^{-10}
2	12.0	3.861×10^{-10}
3	15.86	3.715×10^{-10}
4	27.6	3.539×10^{-10}

When a polymer surface is exposed to high pressure hydrogen, a certain mechanical pressure is exerted on the surface. For the FEM model used in this study, this mechanical pressure can be applied as a boundary condition which is helpful to solve the deformation part of the model. In addition to that, for the diffusion equation, we also need to know how much hydrogen concentration is at the boundary in wt. ppm for a particular value of hydrogen pressure. Without this relation, the PDEs cannot be solved. This relation can be obtained by TDA results. Using fitted Eq. (5) in the TDA results shown in Fig. 6 we can obtain the initial hydrogen concentration value for $t = 0$ using extrapolation. This task was repeated for multiple values of applied pressure and the relation between hydrogen concentration and applied

hydrogen pressure was obtained which is shown using blue circles in Fig. 7. This relation was found to be linear and a trend line was fitted through the points as shown by a red line. The equation of this line was found to be,

$$\text{Pressure (MPa)} = \frac{\text{H}_2 \text{ conc. (in wt. ppm)}}{32}. \tag{25}$$

A line was forced to go through the origin as when no hydrogen pressure is applied, the value of hydrogen concentration must be zero. This relation was used in FEM simulations to apply the corresponding pressure or hydrogen concentration boundary conditions for the coupled model if one is known.

6.2. Simulation results

Fig. 8 shows the spatial distribution of von Mises stress across the deformed shape of the RVE of pure EPDM at different times during the pressurization–depressurization cycle. The amplitude value represents the variation in pressure as well as hydrogen concentration boundary condition P_o and C_o respectively. The highest value of P_o used was 7 MPa and the highest value of C_o was obtained using Eq. (25). At one hour mark, the deformed shape of the RVE shows a dip on the right edge. This is caused due to higher hydrogen pressure on the outside of the cavity than inside as it takes some time for hydrogen to diffuse through the polymer and occupy the cavity void. At five hour mark, the pressure inside the cavity equalizes to outside pressure hence right edge of the cavity becomes straight. As depressurization starts at five hour mark, the outside hydrogen pressure drops to zero within one hour. The trapped hydrogen inside the cavity exerts pressure on the polymer hence a significant blister was formed on the right edge of the cavity which is shown by a black arrow in Fig. 8. This work does not have finite element mesh inside the cavity, therefore modeling the accumulation of gas inside the cavity is challenging. But the expansion of the cavity which caused the bubble formation on the right edge of the RVE can be seen. This is treated as a blister in this study as it is similar to having a blister caused by an accumulation of gas inside the cavity. A blister formation was observed experimentally as well during exposure of hydrogen to the EPDM sample as reported in [64]. A large stress concentration was observed near the periphery of the cavity towards the right edge of the RVE. The trapped hydrogen slowly diffuses out and RVE goes back to its original shape at the ten hour mark.

Fig. 9 shows the spatial distribution of maximum principal strain across the deformed shape of the RVE of pure EPDM at different times during the pressurization–depressurization cycle. Although large strains were observed near the periphery of the cavity towards the right edge of the RVE, maximum principal strain values were still within the critical fracture limit hence no damage was observed.

Similarly, Figs. 10 and 11 show the spatial distribution of hydrogen flux and hydrogen concentration respectively, across the deformed shape of the RVE of pure EPDM at different times during the pressurization–depressurization cycle. After completing the pressurization at one hour mark, the hydrogen concentration near the right edge of RVE was the highest with the lowest concentration on the left side of the cavity. Also, high hydrogen flux was observed on the top and bottom areas of the cavity at the same time. After holding the same pressure for four hours, at five hours mark, an almost uniform hydrogen concentration of 224 wt. ppm was found along with negligible hydrogen flux. Just after finishing depressurization at six hour mark, the lowest hydrogen concentration was observed on the right edge of the RVE. Eventually, all the hydrogen was diffused out by the end of the whole cycle at ten hour mark.

One thing to note here is, under higher hydrogen pressure, if the maximum principal strain value within any finite element exceeds the fracture strain of the material then sudden rupture can be observed. Fig. 12 shows a simulation of the same RVE exposed to 7 MPa with a higher decompression rate of 14 MPa/h. In this case, the value
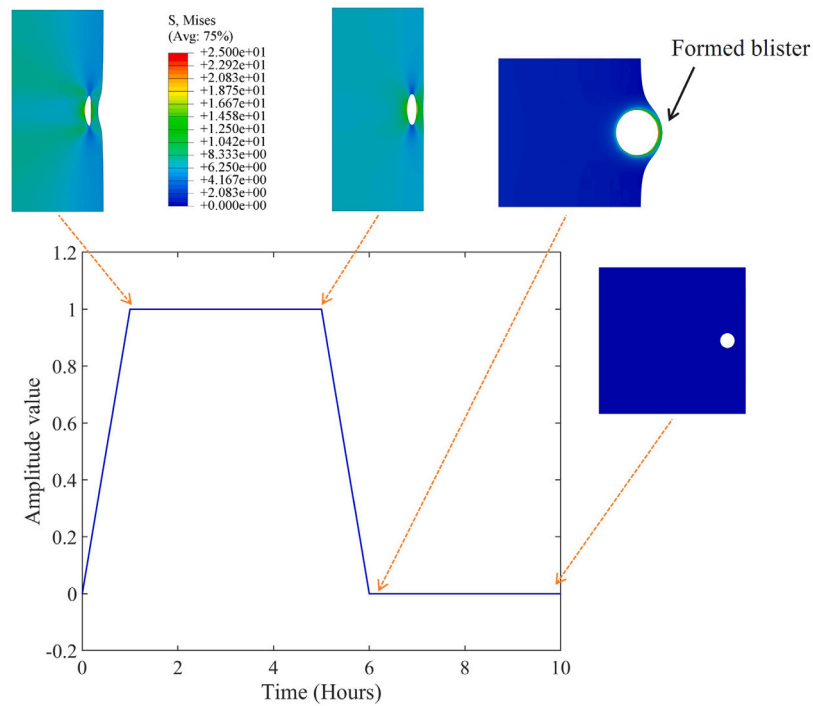
Fig. 8. Spatial distribution of von Mises stress across the RVE of pure EPDM at different times during the pressurization–depressurization cycle.
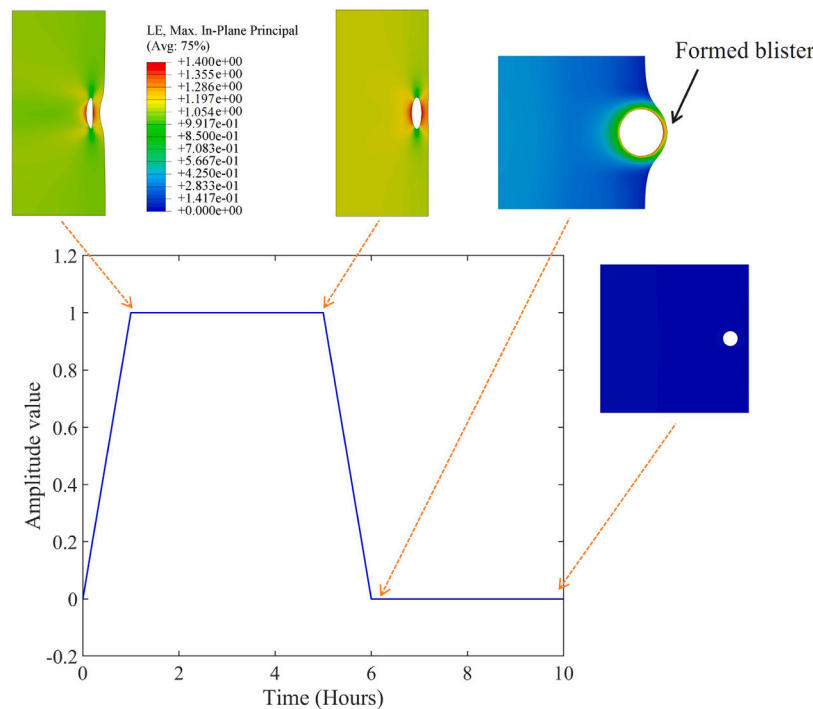

Fig. 9. Spatial distribution of maximum principal strain across the RVE of pure EPDM at different times during the pressurization–depressurization cycle.

of maximum principal strain exceeds the value of fracture stain of 1.39 near the location shown by an arrow in Fig. 12(a). Due to this, corresponding elements got deleted and crack can be seen to initiate. This crack quickly advances towards the surface as shown in Fig. 12(b) resulting in the rapture of polymer. A large amount of elastic strain energy got released due to this sudden rupture causing the stress waves originating near the cavity. Propagation of stress waves from the cavity to the left edge of an RVE can also be seen in Fig. 12(b). This rupture

can also cause the sudden release of hydrogen gas within the polymer to the environment.

We performed simulations of the pressurization–depressurization cycle for three different pressure values of 1.75 MPa, 3.5 MPa, and 7 MPa. During the pressurization phase of the cycle, we observed the same behavior for all three pressure values. But during the depressurization phase of the cycle, RVEs under different pressure values behaved differently. Fig. 13 shows the average hydrogen concentration
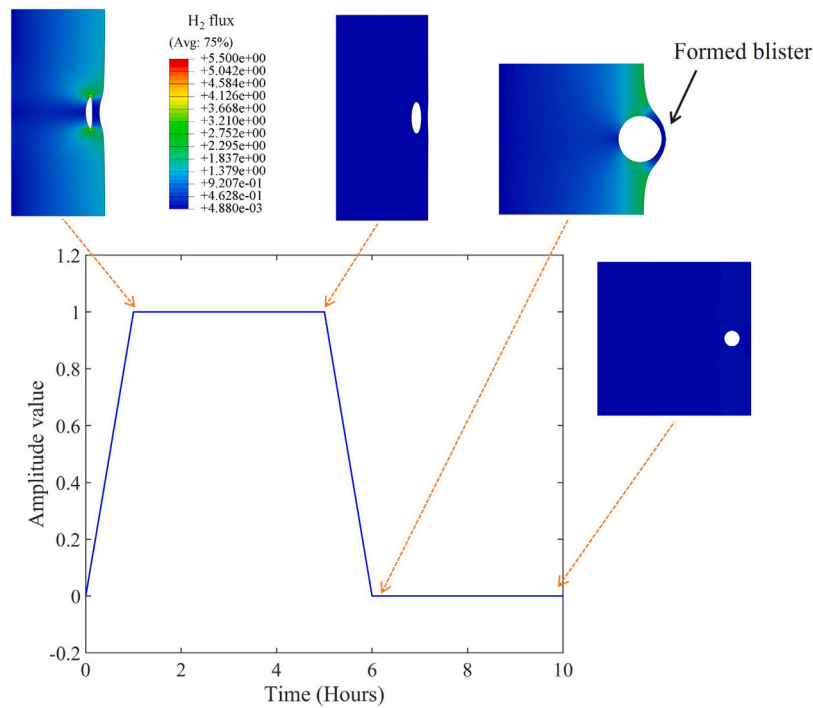
Fig. 10. Spatial distribution of hydrogen flux across the RVE of pure EPDM at different times during the pressurization–depressurization cycle.
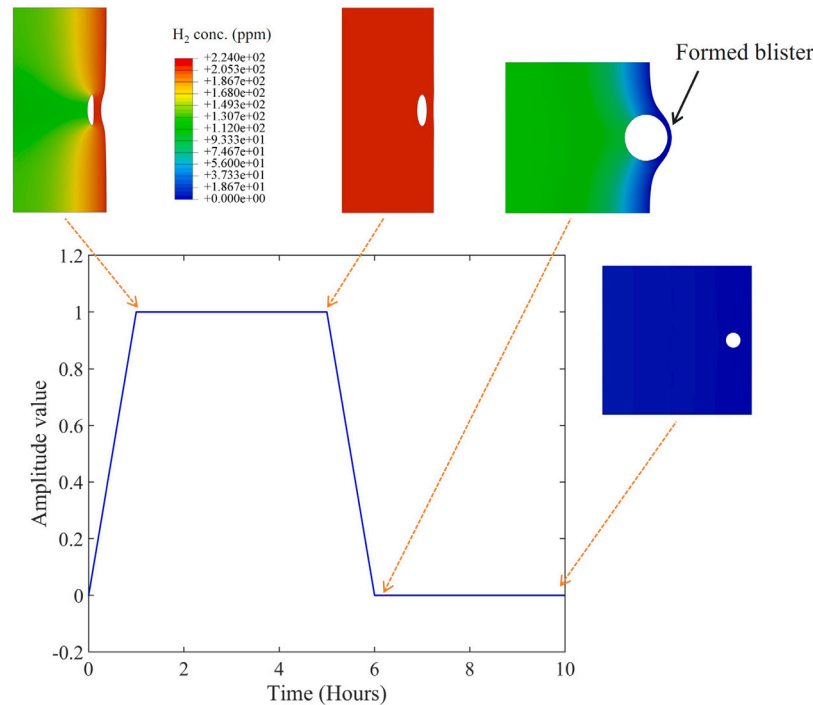

Fig. 11. Spatial distribution of hydrogen concentration across the RVE of pure EPDM at different times during the pressurization–depressurization cycle.

values on the periphery of the cavity during the depressurization phase. It can be observed that as the applied pressure value increases from 1.75 MPa to 7 MPa, the value of hydrogen concentration also increases which is expected. For lower pressures, the hydrogen concentration value monotonically decreases with respect to time but surprisingly for higher pressure values we observed a sudden plateau in the hydrogen concentration value. This trend matches with the experimental results shown in Fig. 6 and shows a hump-like feature.

As seen from Fig. 13, difference between low pressure curves and high pressure curves is the formation of a blister. Fig. 13 also shows the spatial distribution of hydrogen concentration and principal strain across the RVE at the locations shown by arrows. The location was chosen such that the highest pressure (7 MPa) curve has local maxima which was roughly at the middle of the plateau region. The location in the lowest pressure curve was chosen to match the highest pressure location. With multiple simulations, we found that the hump-like feature is observed only when a significant blister is formed on the RVE
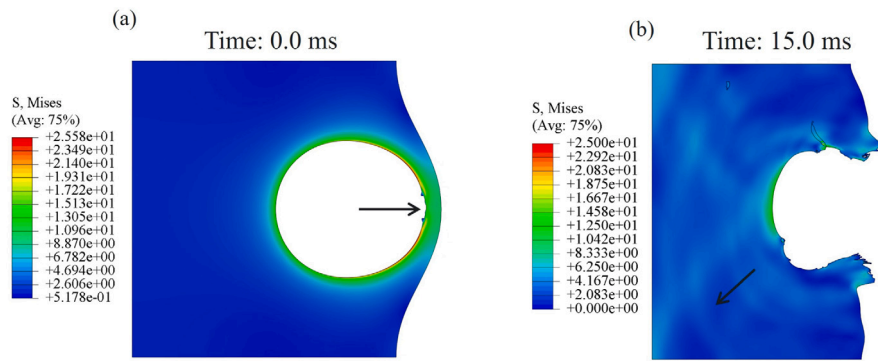
Fig. 12. Results showing (a) damage initiation and (b) damage propagation within RVE during depressurization process.
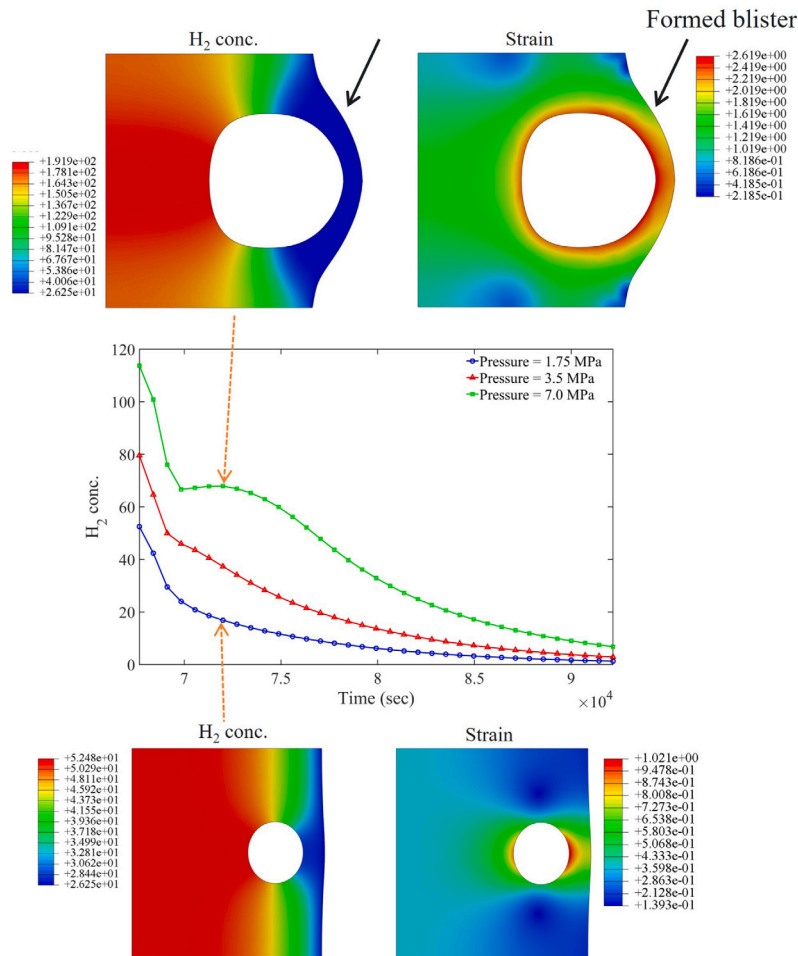

Fig. 13. Results from FEM simulations for different levels of pressurization.

edge. Formation of blister provides an additional resistance for trapped hydrogen gas to diffuse out of the cavity. This additional resistance in path is because of increase in polymer RVE area due to blistering. Rate of decrease in the hydrogen gas in sample again increases as the blister subsides.

We performed the same simulation of the whole pressurization–depressurization cycle with an applied pressure of 7 MPa for three different variants of EPDM namely pure EPDM, plasticized EPDM, and CB filled EPDM. The results for variation of hydrogen concentration with respect to time are given in Fig. 14. It was observed that for CB

filled EPDM, a blister was not formed and hence no hump-like feature was observed. For pure and plasticized EPDM small hump-like feature was observed.

Also, we performed multiple simulations by changing the volume fraction (VF) of the cavity for pure EPDM RVE. Volume fraction was changed by changing the radius of the cavity while keeping its distance from the free surface constant. It was found that for larger cavities, blister formation occurs as a higher amount of hydrogen gas gets trapped inside the cavity during the pressurization phase. This causes blister and hump-like feature which is shown in Fig. 15.
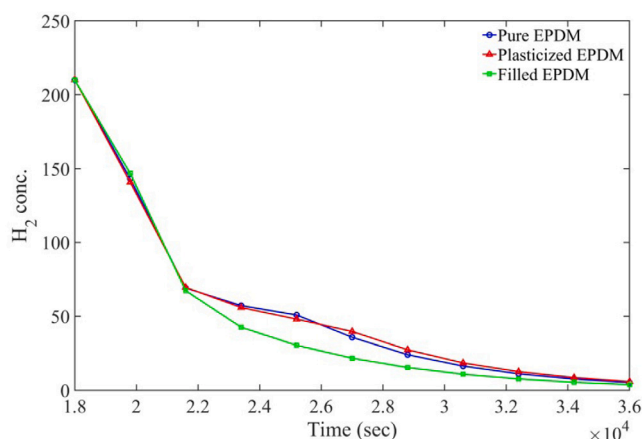
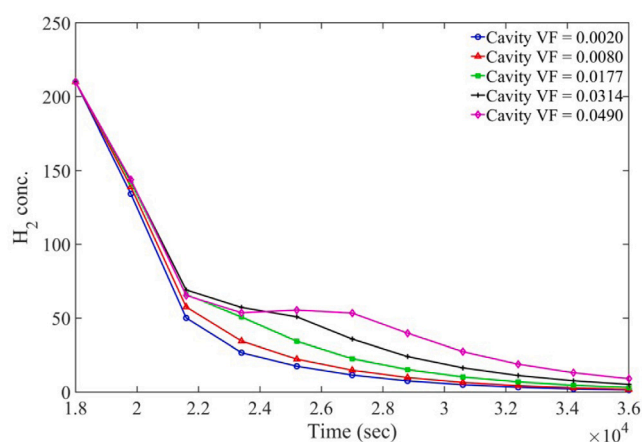**Fig. 14.** Variation of H_2 concentration for different EPDM variants after 7 MPa hydrogen exposure.

Fig. 15. Variation of H_2 concentration for different cavity sizes in pure EPDM after 7 MPa hydrogen exposure.

7. Conclusion

It is crucial to investigate the effect of high pressure hydrogen on rubber like materials to increase the performance of polymer components used in hydrogen infrastructure. Polymers tend to undergo irreversible mechanical damage when exposed high pressure hydrogen is depressurized suddenly. This damage which is also known as rapid decompression failure is one of the main reasons for the failure of polymer components which results in the early replacement of components in service. To avoid such catastrophes in the field, a measurement of hydrogen transport properties in different polymer materials is an important task.

In this study, we used an ex-situ thermal desorption analysis-gas chromatography (TDA-GC) method to measure the coefficient of diffusion of hydrogen through EPDM polymer. The same experiments were repeated for EPDM polymer with added plasticizer and EPDM polymer with added carbon black filler particles and the coefficient of diffusion was measured. The addition of plasticizer was not found to have any effect on the value of the coefficient of diffusion but with the addition of CB filler particles, the coefficient of diffusion was observed to reduce by around 25%. Using Fick's law, the initial hydrogen concentration within the polymer sample was extrapolated for different values of applied hydrogen pressure values. A relation between hydrogen concentration and applied pressure was obtained using these values.

For higher values of applied hydrogen pressure, an anomaly was observed where a sudden increase in the hydrogen retention in the polymer sample was noted. A coupled diffusion–deformation-damage model was deployed to simulate the whole pressurization depressurization cycle where the polymer was modeled as hyperelastic material. Tensile test results were used to obtain the hyperelastic material parameters. All the simulations were performed on the RVE with a size of 2 mm × 2 mm including a circular pre-existing cavity of diameter 0.5 mm. Simulation results revealed that the anomaly in the quantity of hydrogen retention in the sample was due to blister formation on the surface of the sample. A large blister provides an additional resistance for hydrogen to diffuse out which results in an increase in the quantity of hydrogen remaining in the sample. Simulation results also showed that the addition of filler particles in EPDM suppresses the blister formation making the polymer safer against damage.

CRediT authorship contribution statement

Shank S. Kulkarni: Conceptualization, Methodology, Software, Writing – original draft. **Yongsoon Shin:** Validation, Investigation, Writing – review & editing. **Kyoo Sil Choi:** Methodology, Software, Writing – review & editing. **Kevin Simmons:** Project administration, Funding acquisition, Supervision, Writing – review & editing.

Declaration of competing interest

The authors declare that they have no known competing financial interests or personal relationships that could have appeared to influence the work reported in this paper.

Data availability

Data will be made available on request.

Acknowledgments

References

[1] E. Eriksson, E.M. Gray, Optimization and integration of hybrid renewable energy hydrogen fuel cell energy systems–A critical review, Appl. Energy 202 (2017) 348–364.

[2] I. Jain, Hydrogen the fuel for 21st century, Int. J. Hydrogen Energy 34 (17) (2009) 7368–7378.

[3] A. Ajanovic, R. Haas, Economic prospects and policy framework for hydrogen as fuel in the transport sector, Energy Policy 123 (2018) 280–288.

[4] J. Kurtz, S. Sprik, T.H. Bradley, Review of transportation hydrogen infrastructure performance and reliability, Int. J. Hydrogen Energy 44 (23) (2019) 12010–12023.

[5] E. Rivard, M. Trudeau, K. Zaghib, Hydrogen storage for mobility: a review, Materials 12 (12) (2019) 1973.

[6] F. Dawood, M. Anda, G. Shafiullah, Hydrogen production for energy: An overview, Int. J. Hydrogen Energy 45 (7) (2020) 3847–3869.

[7] D.L. Greene, J.M. Ogden, Z. Lin, Challenges in the designing, planning and deployment of hydrogen refueling infrastructure for fuel cell electric vehicles, ETransportation 6 (2020) 100086.

[8] O. Bethoux, Hydrogen fuel cell road vehicles and their infrastructure: An option towards an environmentally friendly energy transition, Energies 13 (22) (2020) 6132.

[9] A. Züttel, Hydrogen storage methods, Naturwissenschaften 91 (4) (2004) 157–172.

[10] L. Zhou, Progress and problems in hydrogen storage methods, Renew. Sustain. Energy Rev. 9 (4) (2005) 395–408.

[11] J. Zheng, X. Liu, P. Xu, P. Liu, Y. Zhao, J. Yang, Development of high pressure gaseous hydrogen storage technologies, Int. J. Hydrogen Energy 37 (1) (2012) 1048–1057.

[12] S.E. Hosseini, B. Butler, An overview of development and challenges in hydrogen powered vehicles, Int. J. Green Energy 17 (1) (2020) 13–37.

[13] J. Woodtli, R. Kieselbach, Damage due to hydrogen embrittlement and stress corrosion cracking, Eng. Fail. Anal. 7 (6) (2000) 427–450.

[14] V. Madina, I. Azkarate, Compatibility of materials with hydrogen. Particular case: Hydrogen embrittlement of titanium alloys, Int. J. Hydrogen Energy 34 (14) (2009) 5976–5980.

[15] K.J. Alvine, V. Shutthanandan, B.W. Arey, C. Wang, W.D. Bennett, S.G. Pitman, Pb nanowire formation on Al/lead zirconate titanate surfaces in high-pressure hydrogen, J. Appl. Phys. 112 (1) (2012) 013533.

[16] M.B. Djukic, V.S. Zeravcic, G.M. Bakic, A. Sedmak, B. Rajicic, Hydrogen damage of steels: A case study and hydrogen embrittlement model, Eng. Fail. Anal. 58 (2015) 485–498.

[17] J. Jaravel, S. Castagnet, J.-C. Grandidier, G. Benoît, On key parameters influencing cavitation damage upon fast decompression in a hydrogen saturated elastomer, Polym. Test. 30 (8) (2011) 811–818.

[18] J. Jaravel, S. Castagnet, J.-C. Grandidier, M. Gueguen, Experimental real-time tracking and diffusion/mechanics numerical simulation of cavitation in gas-saturated elastomers, Int. J. Solids Struct. 50 (9) (2013) 1314–1324.

[19] B. Schrittesser, G. Pinter, T. Schwarz, Z. Kadar, T. Nagy, Rapid Gas Decompression Performance of elastomers–A study of influencing testing parameters, Procedia Struct. Integr. 2 (2016) 1746–1754.

[20] R.R. Barth, K.L. Simmons, C. San Marchi, Polymers for Hydrogen Infrastructure and Vehicle Fuel Systems, Review of Literature and Analysis of Gaps: SAND 89042013, 2013.

[21] J. Pépin, E. Lainé, J.-C. Grandidier, G. Benoit, D. Mellier, M. Weber, C. Langlois, Replication of liner collapse phenomenon observed in hyperbaric type IV hydrogen storage vessel by explosive decompression experiments, Int. J. Hydrogen Energy 43 (9) (2018) 4671–4680.

[22] T.A. Yersak, D.R. Baker, Y. Yanagisawa, S. Slavik, R. Immel, A. Mack-Gardner, M. Herrmann, M. Cai, Predictive model for depressurization-induced blistering of type IV tank liners for hydrogen storage, Int. J. Hydrogen Energy 42 (48) (2017) 28910–28917.

[23] D. Baldwin, Development of High Pressure Hydrogen Storage Tank for Storage and Gaseous Truck Delivery, Tech. rep., Hexagon Lincoln LLC, Lincoln, NE (United States), 2017.

[24] J. Yamabe, S. Nishimura, Influence of fillers on hydrogen penetration properties and blister fracture of rubber composites for O-ring exposed to high-pressure hydrogen gas, Int. J. Hydrogen Energy 34 (4) (2009) 1977–1989.

[25] J. Yamabe, T. Matsumoto, S. Nishimura, Application of acoustic emission method to detection of internal fracture of sealing rubber material by high-pressure hydrogen decompression, Polym. Test. 30 (1) (2011) 76–85.

[26] J. Yamabe, S. Nishimura, Failure behavior of rubber O-ring under cyclic exposure to high-pressure hydrogen gas, Eng. Fail. Anal. 35 (2013) 193–205.

[27] O. Kane-Diallo, S. Castagnet, A. Nait-Ali, G. Benoit, J.-C. Grandidier, Time-resolved statistics of cavity fields nucleated in a gas-exposed rubber under variable decompression conditions–Support to a relevant modeling framework, Polym. Test. 51 (2016) 122–130.

[28] H. Fujiwara, J. Yamabe, S. Nishimura, Evaluation of the change in chemical structure of acrylonitrile butadiene rubber after high-pressure hydrogen exposure, Int. J. Hydrogen Energy 37 (10) (2012) 8729–8733.

[29] H. Fujiwara, H. Ono, S. Nishimura, Degradation behavior of acrylonitrile butadiene rubber after cyclic high-pressure hydrogen exposure, Int. J. Hydrogen Energy 40 (4) (2015) 2025–2034.

[30] S. Castagnet, H. Ono, G. Benoit, H. Fujiwara, S. Nishimura, Swelling measurement during sorption and decompression in a NBR exposed to high-pressure hydrogen, Int. J. Hydrogen Energy 42 (30) (2017) 19359–19366.

[31] H. Ono, A. Nait-Ali, O.K. Diallo, G. Benoit, S. Castagnet, Influence of pressure cycling on damage evolution in an unfilled EPDM exposed to high-pressure hydrogen, Int. J. Fract. 210 (1–2) (2018) 137–152.

[32] K. Ohyama, H. Fujiwara, S. Nishimura, Inhomogeneity in acrylonitrile butadiene rubber during hydrogen elimination investigated by small-angle X-ray scattering, Int. J. Hydrogen Energy 43 (2) (2018) 1012–1024.

[33] S. Castagnet, D. Mellier, A. Nait-Ali, G. Benoit, In-situ X-ray computed tomography of decompression failure in a rubber exposed to high-pressure gas, Polym. Test. 70 (2018) 255–262.

[34] M. Fazal, S. Castagnet, A. Nait-Ali, S. Nishimura, Local kinetics of cavitation in hydrogen-exposed EPDM using in-situ X-Ray tomography: focus on free surface effect and cavity interaction, Polym. Test. 91 (2020) 106723.

[35] A. Koga, K. Uchida, J. Yamabe, S. Nishimura, Evaluation on high-pressure hydrogen decompression failure of rubber O-ring using design of experiments, Int. J. Automot. Eng. 2 (4) (2011) 123–129.

[36] O. Lopez-Pamies, M.I. Idiart, T. Nakamura, Cavitation in elastomeric solids: I—a defect-growth theory, J. Mech. Phys. Solids 59 (8) (2011) 1464–1487.

[37] O. Lopez-Pamies, T. Nakamura, M.I. Idiart, Cavitation in elastomeric solids: II—Onset-of-cavitation surfaces for Neo-Hookean materials, J. Mech. Phys. Solids 59 (8) (2011) 1488–1505.

[38] V. Lefèvre, K. Ravi-Chandar, O. Lopez-Pamies, Cavitation in rubber: an elastic instability or a fracture phenomenon? Int. J. Fract. 192 (1) (2015) 1–23.

[39] X. Poulain, V. Lefevre, O. Lopez-Pamies, K. Ravi-Chandar, Damage in elastomers: nucleation and growth of cavities, micro-cracks, and macro-cracks, Int. J. Fract. 205 (1) (2017) 1–21.

[40] C. Zhou, J. Zheng, C. Gu, Y. Zhao, P. Liu, Sealing performance analysis of rubber O-ring in high-pressure gaseous hydrogen based on finite element method, Int. J. Hydrogen Energy 42 (16) (2017) 11996–12004.

[41] C. Zhou, G. Chen, P. Liu, Finite element analysis of sealing performance of rubber D-ring seal in high-pressure hydrogen storage vessel, J. Fail. Anal. Prev. 18 (4) (2018) 846–855.

[42] S.S. Kulkarni, K.S. Choi, W. Kuang, N. Menon, B. Mills, A. Soulami, K. Simmons, Damage evolution in polymer due to exposure to high-pressure hydrogen gas, Int. J. Hydrogen Energy 46 (36) (2021) 19001–19022.

[43] S.S. Kulkarni, K.S. Choi, K. Simmons, Coupled diffusion-deformation-damage model for polymers used in hydrogen infrastructure, in: International Manufacturing Science and Engineering Conference, Vol. 85819, American Society of Mechanical Engineers, 2022, V002T05A003.

[44] S.S. Kulkarni, K.S. Choi, N. Menon, K. Simmons, A diffusion-deformation model with damage for polymer undergoing rapid decompression failure, J. Mech. Phys. Solids (2023) 105348.

[45] M. Zhang, H. Lv, H. Kang, W. Zhou, C. Zhang, A literature review of failure prediction and analysis methods for composite high-pressure hydrogen storage tanks, Int. J. Hydrogen Energy 44 (47) (2019) 25777–25799.

[46] J.K. Jung, I.G. Kim, K.S. Chung, U.B. Baek, Gas chromatography techniques to evaluate the hydrogen permeation characteristics in rubber: ethylene propylene diene monomer, Sci. Rep. 11 (1) (2021) 1–12.

[47] J.N. Reddy, An Introduction to the Finite Element Method, Vol. 27, New York, 1993.

[48] S.S. Kulkarni, A. Tabarraei, A stochastic analysis of the damping property of filled elastomers, Macromol. Theory Simul. 28 (2) (2019) 1800062.

[49] J. Bonet, R.D. Wood, Nonlinear Continuum Mechanics for Finite Element Analysis, Cambridge University Press, 1997.

[50] E.M. Arruda, M.C. Boyce, A three-dimensional constitutive model for the large stretch behavior of rubber elastic materials, J. Mech. Phys. Solids 41 (2) (1993) 389–412.

[51] M. Mooney, A theory of large elastic deformation, J. Appl. Phys. 11 (9) (1940) 582–592.

[52] R. Rivlin, Large elastic deformations of isotropic materials. IV. Further developments of the general theory, Philos. Trans. R. Soc. Lond. A: Math. Phys. Eng. Sci. 241 (835) (1948) 379–397.

[53] O. Yeoh, Some forms of the strain energy function for rubber, Rubber Chem. Technol. 66 (5) (1993) 754–771.

[54] R.W. Ogden, Large deformation isotropic elasticity–on the correlation of theory and experiment for incompressible rubberlike solids, Proc. R. Soc. Lond. Ser. A Math. Phys. Eng. Sci. 326 (1567) (1972) 565–584.

[55] L. Yang, V. Shim, C. Lim, A visco-hyperelastic approach to modelling the constitutive behaviour of rubber, Int. J. Impact Eng. 24 (6–7) (2000) 545–560.

[56] V. Shim, L. Yang, C. Lim, P. Law, A visco-hyperelastic constitutive model to characterize both tensile and compressive behavior of rubber, J. Appl. Polym. Sci. 92 (1) (2004) 523–531.

[57] O. Barrera, E. Tarleton, H. Tang, A. Cocks, Modelling the coupling between hydrogen diffusion and the mechanical behaviour of metals, Comput. Mater. Sci. 122 (2016) 219–228.

[58] L. Sultanova, Ł. Figiel, Microscale diffusion-mechanics model for a polymer-based solid-state battery cathode, Comput. Mater. Sci. 186 (2021) 109990.

[59] K. Jeong, H.-H. Cho, H.N. Han, D.C. Dunand, A fully coupled diffusional-mechanical finite element modeling for tin oxide-coated copper anode system in lithium-ion batteries, Comput. Mater. Sci. 172 (2020) 109343.

[60] G. Gobbi, C. Colombo, S. Miccoli, L. Vergani, A fully coupled implementation of hydrogen embrittlement in FE analysis, Adv. Eng. Softw. 135 (2019) 102673.

[61] T. Cui, P. Liu, C. Gu, Finite element analysis of hydrogen diffusion/plasticity coupled behaviors of low-alloy ferritic steel at large strain, Int. J. Hydrogen Energy 42 (31) (2017) 20324–20335.

[62] A. Díaz, J. Alegre, I. Cuesta, Coupled hydrogen diffusion simulation using a heat transfer analogy, Int. J. Mech. Sci. 115 (2016) 360–369.

[63] V. Abaqus, 6.14 Documentation, Vol. 651, Dassault Systemes Simulia Corporation, 2014, 6–2.

[64] B.-L. Choi, J.K. Jung, U.B. Baek, B.-H. Choi, Effect of functional fillers on tribological characteristics of acrylonitrile butadiene rubber after high-pressure hydrogen exposures, Polymers 14 (5) (2022) 861.